Miniaturized fiber in-line Mach–Zehnder interferometer based on inner air cavity for high-temperature sensing

T. Y. Hu, Y. Wang, C. R. Liao, and D. N. Wang*

Department of Electrical Engineering, The Hong Kong Polytechnic University, Hung Hom, Kowloon, Hong Kong
**Corresponding author: eednwang@polyu.edu.hk*

Received September 19, 2012; revised October 26, 2012; accepted November 9, 2012;
posted November 9, 2012 (Doc. ID 176539); published December 6, 2012

We demonstrate a miniaturized fiber in-line Mach–Zehnder interferometer based on an inner air cavity adjacent to the fiber core for high-temperature sensing. The inner air cavity is fabricated by femtosecond laser micromachining and the fusion splicing technique. Such a device is robust and insensitive to ambient refractive index change, and has high temperature sensitivity of ~43.2 pm/°C, up to 1000°C, and low cross sensitivity to strain.

OCIS codes: 120.3180, 120.6780, 320.7090.

Optical fiber sensors have been attractive for high-temperature measurement because of their light weight, small size, immunity to electromagnetic interference, and remote sensing capability. Among various types of optical fiber high-temperature sensors developed [1–11], the fiber in-line Mach–Zehnder interferometer (MZI) is of particular interest owing to its high sensitivity. However, such MZI structures reported are mainly based on fiber tapers [9], fiber core diameter mismatch [10], and open air cavity [11], which suffer the drawbacks of large device dimension and/or poor robustness.

A robust MZI structure is reported in [12], which is based on an inner air cavity with a large diameter crossing over the fiber core. However, its output spectrum varies with the surrounding refractive index (RI) fluctuation due to the higher-order cladding modes excited. Although only lower order of cladding modes is excited by a small air hole inside the fiber core [13], a pair of similar air holes needs to be created and separated by a distance of 20 mm, which makes it difficult to measure the temperature at precise location. Moreover, such a temperature sensor exhibits a nonlinear response.

In this Letter, a miniature fiber in-line MZI based on an inner air cavity adjacent to the fiber core is demonstrated for high-temperature sensing at precise location. The air cavity is fabricated by using femtosecond (fs) laser micromachining together with the fusion splicing technique. Light propagating in the fiber core is divided into two portions: one passing through the air cavity and the other traveling along the fiber core, before recombining at the air-cavity end. Compared with the MZI with open air cavity [11,14], the inner air-cavity structure is robust and insensitive to the surrounding RI variation.

Figure 1 shows the schematic structure of the device. The abrupt core bending imposed by the air cavity leads to the transition from the core mode to the cavity mode and the cladding mode. After the cladding mode is largely suppressed by the microstructure created on the inner surface of the air cavity, the input light is split into two portions by the air cavity, denoted by I_{in1} and I_{in2}, respectively. I_{in1} travels via the air cavity, I_{in2} remains propagating within the fiber core, and interference happens when the two output beams, I_{out1} and I_{out2}, recombine in the fiber core, at the air-cavity end. The MZI output intensity can be written as

$$I = I_{\text{out1}} + I_{\text{out2}} + 2\sqrt{I_{\text{out1}} I_{\text{out2}}}\cos\left(\frac{2\pi L \Delta n_{\text{eff}}}{\lambda} + \varphi_0\right), \quad (1)$$

where λ is the wavelength of the incident light, L is the air-cavity length, $\Delta n_{\text{eff1}} = n_{\text{eff}}^{\text{core}} - n_{\text{eff}}^{\text{cavity}}$ is the effective RI difference between the core mode and the air-cavity mode, and φ_0 is the initial phase of the interference. Assuming that L is a constant, the temperature sensitivity of the MZI can be derived from Eq. (1) as

$$\frac{d\lambda}{dT} = \frac{\lambda}{n_{\text{eff}}^{\text{core}}(T) - n_{\text{eff}}^{\text{cavity}}(T)}\left(\frac{dn_{\text{eff}}^{\text{core}}(T)}{dT} - \frac{dn_{\text{eff}}^{\text{cavity}}(T)}{dT}\right), \quad (2)$$

where $dn_{\text{eff}}^{\text{core}}(T)/dT$ and $dn_{\text{eff}}^{\text{cavity}}(T)/dT$ are temperature coefficients of the RI of fiber core and air, respectively. Note that $n_{\text{eff}}^{\text{cavity}}$ remains constant for different temperatures; hence the sensitivity of the MZI is determined by the temperature coefficient of the fiber core RI.

In the device fabrication, fs laser pulses ($\lambda = 800$ nm) of 120 fs at the repetition rate of 1 kHz were focused onto the fiber by a 20× objective lens with an NA value of 0.50 and a working distance of 2.1 mm. A CCD camera was employed to monitor the fabrication process and record the sample morphology. A standard single mode fiber (SMF)-28 with the core diameter of 8.2 μm and the nominal effective RI of 1.4682 (at 1550 nm) was mounted on a computer-controlled three-dimensional translation stage with a 40 nm resolution. A microsquare structure with the side length of ~20 μm and the largest depth of ~23 μm, centered at 15 μm away from the center of the fiber axis,

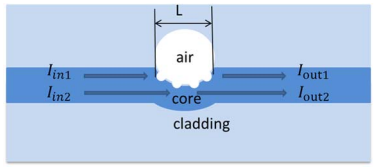

Fig. 1. (Color online) Schematic diagram of the fiber in-line MZI proposed.

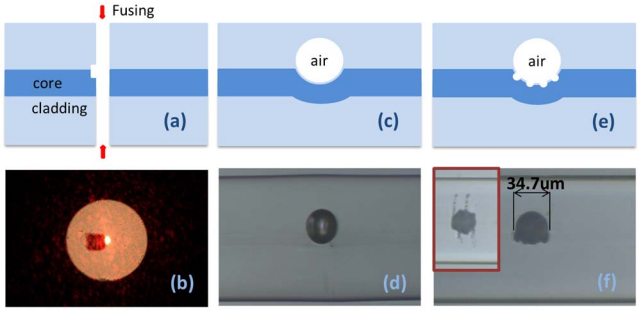

Fig. 2. (Color online) Illustration of the fiber in-line MZI fabrication process. (a) Microstructure created at the end of fiber tip. (b) Microscope image of the fiber tip with microsquare structure. (c) Air cavity adjacent to the fiber core formed in SMF. (d) Microscope image of the air-cavity formed in SMF. (e) The air cavity with microstructure. (f) Microscope images of the side view and top view (inset) of the air cavity with microstructure.

was inscribed by fs laser pulses with the energy of ~3 μJ, as shown in Fig. 2(a). The microscope image of the cross-section view of the fiber tip with the microsquare structure is displayed in Fig. 2(b). The fiber tip with microstructure was then fusion spliced together with another cleaved SMF tip to create a hollow sphere adjacent to the fiber core as demonstrated in Fig. 2(c), which essentially formed an MZI. Figure 2(d) provides the microscope image of the hollow sphere obtained. The fusion splicer used was ERICSSO FSU975, and the fusing current and fusing duration employed were 14.3 mA and 1.5 s, respectively. Besides the fundamental core mode and the air-cavity mode, higher-order cladding modes are also excited by the air cavity, which leads to multiple beam interference and, as the higher-order cladding modes propagate near the fiber surface, the interferometer output is sensitive to the surrounding RI variation. To suppress the higher-order cladding mode, the microstructure on the inner surface of the air cavity as shown in Fig. 2(e) was fabricated by fs laser micromachining, which consisted of four parallel lines across the air cavity and fiber core boundary. Figure 2(f) and its inset show the microscope image of the side view and the top view of the air cavity with such a microstructure, respectively. In the microstructure fabrication process, the fs laser pulses with pulse energy of 1.5 μJ were focused onto the air cavity inner surface adjacent to the fiber core and scanned at a speed of 200 μm/s across the fiber diameter, perpendicular to the fiber axis, to create a microline structure at the edge of the air cavity. The laser beam was then shifted by 10 μm, parallel to the fiber axis, and started a new scanning cycle until a four microline structure was produced on the inner surface of the air cavity. As shown in the inset of Fig. 2(f), clear tracks were formed along the scanning paths when the focused laser beam was moving from the air cavity into the silica bulk. This is due to the fact that the surface damage threshold of fused silica at the air-dielectric interface is much lower than that in the bulk [15]. Once the focused beam intensity is lower than the bulk damage threshold but higher than that of the surface, defects are formed in the vicinity of the focal spot when the laser beam crosses the air-cavity interface. Such defects lower the local damage threshold of the adjacent materials along the laser scanning path.

The impact of inscribed microstructure on the inner surface of the air cavity is illustrated in Fig. 3. The MZI output spectrum corresponding to the air cavity without microstructure contains two sets of fringes: the one with a large free spectral range (FSR) is produced by the interference between the core mode and the air-cavity mode, and the other with a small FSR value of 40 nm is due to the interference between the higher-order cladding mode and the core mode. As both the intensities of the air cavity mode and the cladding modes are very small when compared with that of the core mode, the interference between the air-cavity mode and higher-order cladding mode can be ignored. When the microstructure is introduced on the inner surface of the air cavity, a small dip wavelength shift is observed for the fringe pattern with larger FSR, together with a large visibility

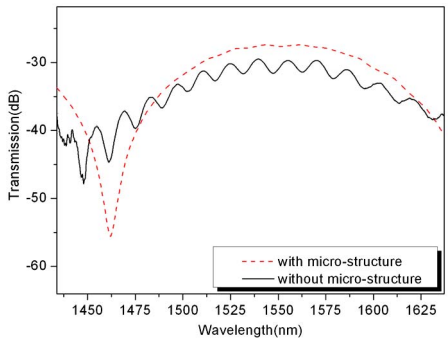

Fig. 3. (Color online) Interference spectrum with or without microstructure on the inner surface of the air cavity.

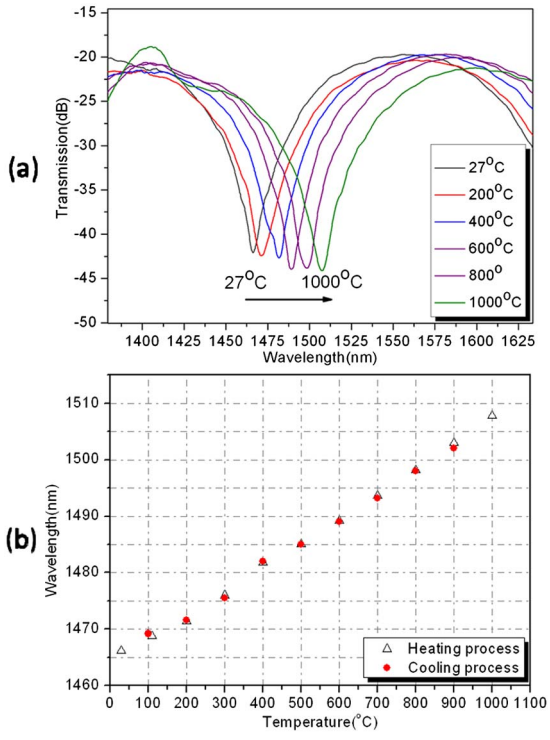

Fig. 4. (Color online) (a) Interference spectra of the fiber in-line fiber MZI at different temperatures. (b) Interference dip wavelength versus temperature.

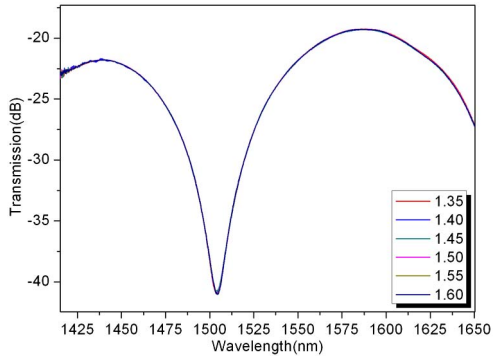

Fig. 5. (Color online) Interference spectra of the in-line fiber MZI immersed in different RI liquids.

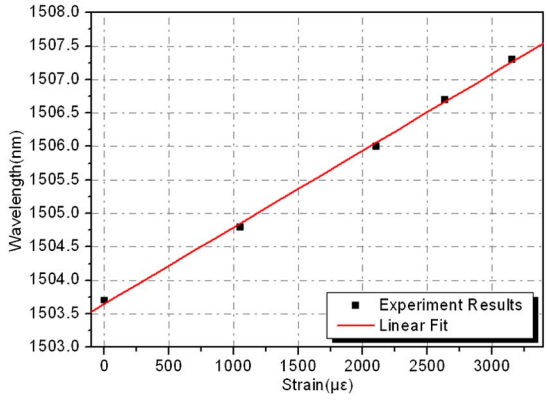

Fig. 6. (Color online) Interference dip shift versus strain.

improvement, due to the fact that part of the core mode is excited into the air-cavity mode. More importantly, the fringe pattern with smaller FSR almost totally disappears as the higher-order cladding modes are excited into the radiation modes.

The temperature measurement of the device is implemented by use of a tubular furnace. First, the sensor was heated from room temperature (27°C) to 1000°C at an average rate of 5°C/min, and stayed at 1000°C for 3 h to remove the burnt fiber coating-induced effects before being cooled down to room temperature. The temperature was then gradually increased to 100°C, and from 100°C to 1000°C with a step of 100°C, stayed for 20 min at each step. The sensor was kept at 1000°C for 30 min before being cooled down to 100°C, following the same step and staying time as in the heating process. Figure 4(a) shows the transmission spectra at a number of temperature points and a clear red shift of fringe dip wavelength with the increase of temperature can be observed. The fringe dip wavelength shift with the temperature change is displayed in Fig. 4(b), where a good repeatability in both the heating and the cooling processes can be found and the temperature sensitivity obtained is ~43.2 pm/°C.

The response of the MZI to the ambient RI change was examined by immersing the device in the liquids with RI values ranging from 1.35 to 1.60. Figure 5 shows the transmission spectra of the MZI in different RI liquids. The nearly unchanged spectrum reveals the insensitivity of the device to the surrounding RI.

The response of the MZI to the axial strain was also tested in the range between 0 and 3157 με and the results obtained are shown in Fig. 6. The strain sensitivity obtained is only ~1.15 pm/με owing to the small inner air cavity in the SMF, which makes the strain cross sensitivity small as 0.0266°C/με. The wide strain measurement range up to 3157 με also indicates the robustness of the device.

In summary, a fiber in-line MZI based on an inner air cavity adjacent to fiber core is developed for high-temperature sensing. The inner air cavity is fabricated by fs laser micromachining together with the fusion splicing technique. The influence of the higher cladding mode can be eliminated and hence the RI cross sensitivity can be removed by introducing microstructure on the inner surface of the air cavity. The device exhibits a high temperature sensitivity of ~43.2 pm/°C up to 1000°C and a small strain cross sensitivity of ~0.0266°C/με. The fiber in-line MZI sensor developed is miniature and robust, with high-temperature sensitivity and low external RI and strain cross sensitivities.

References

1. G. Brambilla and H. Rutt, Appl. Phys. Lett. **80**, 3259 (2002).
2. D. Grobnic, C. W. Smelser, S. J. Mihailov, and R. B. Walker, Meas. Sci. Technol. **17**, 1009 (2006).
3. Y. Li, M. Yang, C. R. Liao, D. N. Wang, J. Lu, and P. X. Lu, IEEE J. Lightwave Technol. **29**, 1555 (2011).
4. V. Bhatia and A. M. Vengsarkar, Opt. Lett. **21**, 692 (1996).
5. S. Bandyopadhyay, J. Canning, M. Stevenson, and K. Cook, Opt. Lett. **33**, 1917 (2008).
6. Y. Zhu, P. Shum, H. Bay, M. Yan, X. Yu, J. Hu, J. Hao, and C. Lu, Opt. Lett. **30**, 367 (2005).
7. Y. Zhu, Z. Huang, F. Shen, and A. Wang, Opt. Lett. **30**, 711 (2005).
8. H. Y. Choi, K. S. Park, S. J. Park, U. C. Paek, B. H. Lee, and E. S. Choi, Opt. Lett. **33**, 2455 (2008).
9. D. Monzón-Hernández, V. P. Minkovich, and J. Villatoro, IEEE Photon. Technol. Lett. **18**, 511 (2006).
10. L. V. Nguyen, D. Hwang, S. Moon, D. S. Moon, and Y. Chung, Opt. Express **16**, 11369 (2008).
11. Y. Wang, Y. Li, C. Liao, D. N. Wang, M. Yang, and P. Lu, IEEE Photon. Technol. Lett. **22**, 39 (2010).
12. M. Park, S. Lee, W. Ha, D. K. Kim, W. Shin, I. B. Sohn, and K. Oh, IEEE Photon. Technol. Lett. **21**, 1027 (2009).
13. L. Jiang, J. Yang, S. Wang, B. Li, and M. Wang, Opt. Lett. **36**, 3753 (2011).
14. Y. Wang, M. Yang, D. N. Wang, S. Liu, and P. Lu, J. Opt. Soc. Am. B **27**, 370 (2010).
15. C. B. Schaffer, A. Brodeur, and E. Mazur, Meas. Sci. Technol. **12**, 1784 (2001).